

Stochastic Design of Active RIS-Assisted Satellite Downlinks under Interference, Folded Noise, and EIRP Constraints

Muhammad Khalil, *Member, IEEE*, Ke Wang, *Senior Member, IEEE*, and Jinho Choi, *Fellow, IEEE*

Abstract

Active reconfigurable intelligent surfaces (RISs) can mitigate the double-fading loss of passive reflection in satellite downlinks, but their benefits are limited by random cochannel interference, gain-dependent amplifier noise, and regulatory emission constraints. This paper develops a stochastic reliability framework for active RIS-assisted satellite downlinks by modeling the desired and interfering channels, receiver noise, and RIS amplifier noise as random variables, leading to an instantaneous Signal-to-Interference-plus-Noise Ratio (SINR) representation that explicitly captures folded (cascaded) amplifier noise. The resulting model reveals a finite high-gain SINR ceiling.

To guarantee a target outage probability, we formulate a chance-constrained max-SINR design that jointly optimizes the binary RIS configuration and the common amplification gain. The chance constraint is handled via a sample-average approximation (SAA) with a violation budget, and the resulting feasibility problem is solved as a mixed-integer second-order cone program (MISOCP) within a bisection search over the SINR threshold. Practical implementability is ensured by restricting the gain to the admissible range imposed by small-signal stability and effective isotropic radiated power (EIRP) limits. In addition, we derive realization-wise SINR envelopes based on eigenvalue and ℓ_1 bounds, which provide interpretable performance limits and fast diagnostics.

Monte Carlo results confirm that the envelopes tightly bracket the simulated SINR, reproduce the predicted saturation behavior, and quantify performance degradation as interference increases. These results provide a solver-ready, reliability-targeting design methodology whose achieved reliability is validated via Monte-Carlo testing for active RIS-assisted satellite downlinks under realistic randomness and hardware constraints.

Index Terms

RIS, satellite, amplifier noise, reliability analysis.

Table I
MAIN CONTRIBUTIONS OF THE PAPER.

#	Title	Key ideas & significance
C1	Stochastic SINR Bounds for Active RIS-Satellite Links	Derives simple closed-form SINR upper/lower bounds that hold for each random channel realization, capturing fading, multi-satellite interference, and active-RIS amplification effects. <i>Impact:</i> Enables fast reliability assessment without extensive Monte Carlo simulation.
C2	Reliability-Targeting Joint Design	Poses a chance-constrained joint design of discrete RIS phases and a continuous active-RIS gain targeting an SINR non-outage level $1 - \epsilon$ under stochastic fading and interference, and solves an SAA-MISOCP approximation whose achieved reliability is validated via out-of-sample Monte-Carlo evaluation. <i>Impact:</i> Solver-ready reliability-targeting configuration under practical gain (stability/EIRP) limits.
C3	Folded-Noise Modeling and SINR Ceiling Law	Introduces a gain-dependent folded-noise model that captures how amplifier noise propagates through the RIS-assisted link, and proves a finite reliability-guaranteed SINR ceiling under stochastic interference, implying that increasing g beyond a threshold yields diminishing (or no) returns. <i>Impact:</i> Explains why active-RIS amplification saturates and when the link becomes noise-limited.
C4	Hardware- and Regulation-Compliant Design Constraints	Integrates amplifier stability and EIRP regulations directly into the reliability-aware optimization via convex reformulations, ensuring implementable solutions under physical hardware limits. <i>Impact:</i> Enables certifiable active-RIS operation under practical stability/EIRP constraints in satellite downlinks.

I. INTRODUCTION

Reconfigurable intelligent surfaces (RISs) have emerged as a practical way to shape wireless propagation and improve coverage in future networks [1]. By using electronically tunable reflecting elements, an RIS can coherently reconfigure incident waves and enhance the received signal without additional RF chains [2]. Early studies showed that, under favorable geometry (e.g., blockage scenarios), the received power can scale roughly with the square of the number of RIS elements [3]. Subsequent analyses incorporated fading and quantified performance via SINR/outage distributions, confirming the reliability improvements enabled by RIS-assisted virtual line-of-sight paths [4]. These advances have motivated broad investigations of RISs for coverage extension, physical-layer security, and localization, with surveys emphasizing their spectral-and energy-efficiency potential for beyond-5G/6G systems [5]–[8].

Motivated by these terrestrial results, RIS-assisted architectures are also being explored for

non-terrestrial and satellite communications. Multibeam SatCom with aggressive frequency reuse offers high throughput and wide-area service; however, it is limited by severe path loss and co-channel interference due to beam overlap [9]. Introducing an RIS into the satellite downlink can provide a controllable reflection path to mitigate shadowing and strengthen the received signal [10]. For example, [11] reports improved sum-rate and coverage in RIS-aided multibeam GEO systems, while [12] derives outage and rate expressions for an RIS-assisted LEO scenario using a UAV-mounted reflector, demonstrating gains over obstructed direct links. Overall, these works indicate that RISs can complement SatCom by extending coverage into deep fades and coverage holes.

Most existing RIS studies in both terrestrial and SatCom settings focus on *passive* surfaces that only apply controllable phase shifts. Although power-efficient, passive RISs suffer from a *multiplicative (double-fading)* limitation: the end-to-end gain is the product of the transmitter–RIS and RIS–receiver links, which can be especially weak when the two-hop path loss is large or a strong direct path exists [13]. This is critical for satellite downlinks, where long satellite–RISs and RIS–user distances compound attenuation, so passive RISs often provide modest SINR/rate gains unless very large apertures are used or the direct link is blocked [14]. Empirical findings report only limited improvement in typical LoS terrestrial deployments [15], and SatCom studies further note that passive reflections may also reradiate co-channel interference from adjacent beams, thereby reducing the net benefit under full-frequency reuse [16].

To overcome these limitations, *active* RIS architectures embed low-power amplifiers in each element to boost the reflected signal and partially compensate for the double-fading loss [17], [18]. Prototype results indicate that active reflection can surpass passive capacity ceilings by injecting power into the reradiated link [19]. However, amplification introduces new constraints: amplifier noise and distortion are folded through the cascaded channel, so increasing gain eventually yields diminishing SINR returns and a finite high-gain ceiling [20]–[24]. In addition, practical operation must satisfy small-signal stability and regulatory EIRP limits, as excessive gain can trigger oscillations or violate emission constraints [25], [26]. Recent work has therefore studied active-RIS designs with joint beamforming/coefficients and architectures that limit noise accumulation and out-of-band radiation [27]–[30], as well as security-oriented applications [31]. In SatCom, active RIS concepts are still nascent; early studies suggest coverage gains in deep fades/NLoS (e.g., UAV-mounted active RISs) [32], [33], but most analyses assume simplified links (often single-user or interference-free) and ideal gain control, leaving reliability-aware

design under realistic multi-beam interference and stochastic fading largely open.

These observations motivate a unified design framework for active RIS-assisted satellite downlinks that jointly capture *stochastic fading*, *co-channel interference*, and *hardware-induced noise*. Most optimization-driven RIS designs (passive or active) adopt deterministic links and idealized channel knowledge, targeting average or worst-case metrics [34]. In practice, satellite channels are highly time-varying due to user mobility, satellite motion, and atmospheric effects, while interference fluctuates with geometry and traffic load. Hence, guaranteeing a consistent quality-of-service requires a *reliability-driven* formulation [35]. Chance-constrained methods are a standard tool for enforcing probabilistic SINR/outage guarantees in robust communications [36], and initial RIS studies have incorporated outage behavior via SNR/SINR distributions and phase design [12]. However, a unified framework that *jointly* optimizes discrete RIS states (e.g., binary phase shifts) and continuous active gains under probabilistic SINR constraints, while explicitly enforcing stability and EIRP limits, is still missing. This gap motivates our work.

In this paper, we develop a stochastic optimization framework for an active RIS-assisted satellite downlink under random fading and co-channel interference. The main contributions are as follows: (i) we establish a stochastic SINR model in which desired and interfering channels, as well as both receiver thermal noise and RIS amplifier noise, are treated as random variables; (ii) we pose a reliability-aware design via a chance constraint on the SINR and derive a tractable sample-average approximation (SAA) solved by a mixed-integer second-order cone program (MISOCP); (iii) we introduce a folded, gain-dependent noise model that explains SINR saturation at high gains; and (iv) we embed practical hardware and regulatory constraints—small-signal stability and EIRP limits—directly into the optimization, ensuring physically realizable designs. The major contributions are summarized in Table I.

The remainder of this paper is organized as follows. Section II presents the stochastic system model (Rician block fading, binary RIS reflection, and gain-dependent folded noise). Section III formulates a chance-constrained reliability design and derives an SAA-based MISOCP to jointly optimize the RIS phases and gain. Section IV develops interference-aware SINR envelopes and the high-gain ceiling under amplifier noise. Section V provides numerical validation under stability/EIRP-limited gain and explores reliability over (N, M, g) . Section VI concludes and outlines extensions to dual-band operation, data-driven RIS control, and measured channels.

II. SYSTEM MODEL (STOCHASTIC)

We consider a narrowband satellite downlink assisted by an *active* RIS, as illustrated in Fig. 1. One desired satellite transmits to a ground receiver, while M neighboring satellites reuse the same carrier, creating cochannel interference. The satellite–RIS, RIS–receiver, and direct satellite–receiver channels follow a block-fading model: the channel coefficients remain constant within each coherence block and change independently from one block to the next. Throughout, the fading coefficients and noise terms are modeled as random variables.

Model components:

- **Topology:** one desired satellite, M cochannel interferers, one active RIS with N elements, and a ground receiver with combiner \mathbf{w} (Fig. 1).
- **Channels:** block-fading Rician links (satellite–RIS, RIS–receiver, and satellite–receiver) [11], [12].
- **Active RIS:** two-state phase control $\mathbf{b} \in \{\pm 1\}^N$ and common gain g [17], [19].
- **Noise:** receiver thermal noise and gain-dependent RIS amplifier noise folded through $\mathbf{H}_r(\cdot)$ [20], [21].

The desired satellite employs a fixed precoder $\mathbf{f} \in \mathbb{C}^{N_t}$, and the ground receiver applies a linear combiner $\mathbf{w} \in \mathbb{C}^{N_r}$. The interferer m uses \mathbf{f}_m . The transmitted symbols are modeled as zero-mean proper complex Gaussian:

$$x \sim \mathcal{CN}(0, P_d), \quad x_m \sim \mathcal{CN}(0, P_m),$$

independent across transmitters and independent of all noise sources and channels.

Each hop (satellite → RIS, RIS → receiver, and satellite → receiver) follows a Rician law with elevation-dependent path LoS and a Rician K -factor $K(\varepsilon) \geq 0$, defined as the ratio between the average power in the deterministic LoS component and the average power in the scattered NLoS component.

$$\mathbf{H}(\omega) = \sqrt{\beta_{\text{fs}}(s, \lambda)} \left(\sqrt{\frac{K(\varepsilon)}{K(\varepsilon)+1}} \mathbf{H}_{\text{LoS}} + \sqrt{\frac{1}{K(\varepsilon)+1}} \mathbf{H}_{\text{NLoS}}(\omega) \right), \quad (1)$$

where $\beta_{\text{fs}}(s, \lambda) = (4\pi s/\lambda)^{-2}$ captures free-space path loss. $\mathbf{H}_{\text{NLoS}}(\omega)$ has i.i.d. $\mathcal{CN}(0, 1)$ entries, and \mathbf{H}_{LoS} is the deterministic array response. For the desired link, we denote $\mathbf{H}_d(\omega)$ (direct path), $\mathbf{G}_t(\omega)$ (satellite→RIS), and $\mathbf{H}_r(\omega)$ (RIS→receiver). For the interferers m , we use $\mathbf{H}_{d,m}(\omega)$ and $\mathbf{G}_{t,m}(\omega)$. All satellites illuminate the same RIS, so $\mathbf{H}_r(\omega)$ is common.

Each RIS element applies a binary phase reflection (0 or π) and a common small-signal gain g , scaled by the passive retention factor ρ . This captures a simple yet practical two-state phase control with a uniform amplifier setting across the array, consistent with first-generation active RIS prototypes [19]. Specifically,

$$\Gamma_i = \alpha b_i, \quad \alpha = \rho g, \quad b_i \in \{+1, -1\}, \quad i = 1, \dots, N,$$

where $0 < \rho \leq 1$ models passive retention and $g \geq 0$ is the active gain. Let $\mathbf{b} = [b_1, \dots, b_N]^\top$ and $\mathbf{\Gamma} = \alpha \text{diag}(\mathbf{b})$.

To calculate the cascaded coefficients, let $\mathbf{h}_{r,i}(\omega)$ denote the i -th column of the RIS–receiver channel $\mathbf{H}_r(\omega)$, and let $\mathbf{g}_{t,i}(\omega)$ denote the i -th row of the satellite–RIS channel $\mathbf{G}_t(\omega)$. The corresponding random complex scalars are

$$d(\omega) = \mathbf{w}^\text{H} \mathbf{H}_d(\omega) \mathbf{f}, \quad u_i(\omega) = (\mathbf{w}^\text{H} \mathbf{h}_{r,i}(\omega)) (\mathbf{g}_{t,i}^\top(\omega) \mathbf{f}), \quad (2)$$

and the vector of RIS–mediated coefficients is $\mathbf{u}(\omega) = [u_1(\omega), \dots, u_N(\omega)]^\top$. For the m -th interferer, the same construction applies after replacing $(\mathbf{H}_d, \mathbf{G}_t, \mathbf{f})$ with $(\mathbf{H}_{d,m}, \mathbf{G}_{t,m}, \mathbf{f}_m)$, yielding $d_m(\omega)$ and $\mathbf{u}_m(\omega)$.

To account for the receiver and RIS noise, note that the receiver thermal disturbance is $\mathbf{n}_r \sim \mathcal{CN}(\mathbf{0}, N_0 \mathbf{I})$. Each RIS element also introduces an independent or correlated amplifier noise term $\mathbf{n}_{\text{RA}}(\omega) \in \mathbb{C}^N$, modeled as a zero-mean proper complex Gaussian with covariance

$$\mathbb{E}[\mathbf{n}_{\text{RA}}(\omega) \mathbf{n}_{\text{RA}}^\text{H}(\omega)] = \mathbf{\Sigma}_a(g, \omega) \succeq \mathbf{0}.$$

A convenient small-signal law expresses the per-element variance as $\sigma_a^2(g) = \sigma_{\min}^2 + \eta g^2$, leading to $\mathbf{\Sigma}_a(g, \omega) = \sigma_a^2(g) \mathbf{R}_a(\omega)$, where $\mathbf{R}_a(\omega) = \mathbf{I}$ represents the i.i.d. case and the non-diagonal $\mathbf{R}_a(\omega)$ captures spatial correlation.

After propagation through the RIS–receiver channel $\mathbf{H}_r(\omega)$ and combining by \mathbf{w} , the total folded noise variance is

$$\text{Var}(\mathbf{w}^\text{H} \mathbf{H}_r(\omega) \mathbf{n}_{\text{RA}}(\omega)) = \mathbf{w}^\text{H} \mathbf{H}_r(\omega) \mathbf{\Sigma}_a(g, \omega) \mathbf{H}_r^\text{H}(\omega) \mathbf{w}. \quad (3)$$

Here, *folded noise* refers to the amplifier noise generated across the RIS elements, which propagates through $\mathbf{H}_r(\omega)$ and is spatially combined by \mathbf{w} , thereby *folding* the spatial noise field at the RIS into an effective noise contribution at the receiver output.

For the common i.i.d. specialization, $\mathbf{\Sigma}_a(g, \omega) = \sigma_a^2(g) \mathbf{I}$ with $\sigma_a^2(g) = \sigma_{\min}^2 + \eta g^2$, the folded-noise variance reduces to $\sigma_a^2(g) L(\omega)$, where $L(\omega) = \|\mathbf{H}_r^\text{H}(\omega) \mathbf{w}\|_2^2$ quantifies the combiner–RIS channel alignment.

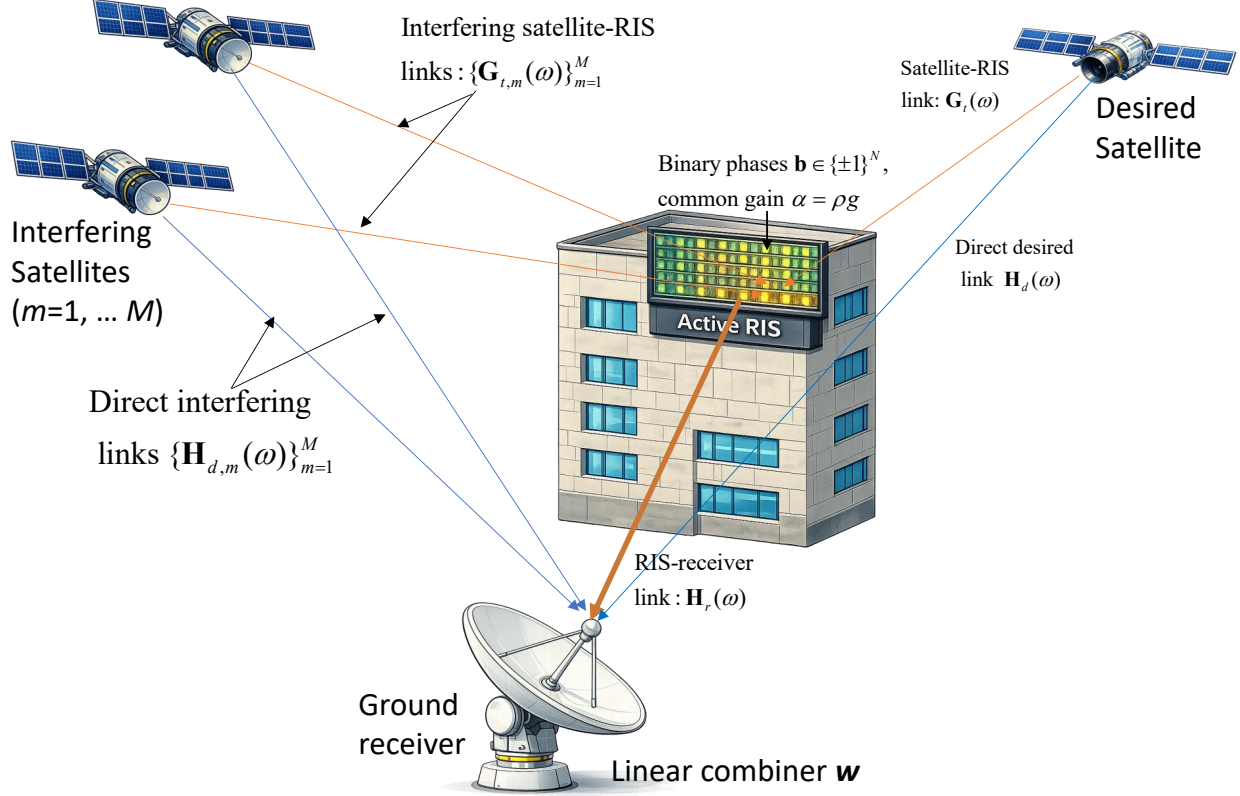


Fig. 1. Active RIS-assisted satellite downlink with one desired satellite and M cochannel interferers. Desired and interfering signals reach the ground receiver via direct links $\mathbf{H}_d(\omega)$ and $\{\mathbf{H}_{d,m}(\omega)\}$ and via the RIS-assisted paths through $\mathbf{G}_t(\omega)$, $\{\mathbf{G}_{t,m}(\omega)\}$, and $\mathbf{H}_r(\omega)$. Blue links denote desired propagation; red links denote interference.

After accounting for the aforementioned channel and noise components, the scalar received signal during one coherence block can be expressed as follows:

$$\begin{aligned}
 y(\omega) = & \left(d(\omega) + \rho g \mathbf{u}^\top(\omega) \mathbf{b} \right) x + \sum_{m=1}^M \left(d_m(\omega) + \rho g \mathbf{u}_m^\top(\omega) \mathbf{b} \right) x_m \\
 & + \mathbf{w}^\top \mathbf{n}_r + \mathbf{w}^\top \mathbf{H}_r(\omega) \mathbf{n}_{RA}(\omega).
 \end{aligned} \tag{4}$$

Here, the first term represents the desired signal reflected by the RIS, the summation accounts for cochannel interference from M neighboring satellites, and the last two terms correspond to the receiver thermal noise and folded amplifier noise from the RIS, respectively.

To obtain a phase-aligned representation, let $\phi(\omega) = \arg(d(\omega))$ denote the instantaneous phase of the direct component. By rotating all reflected terms by $e^{-j\phi(\omega)}$, we define $\tilde{\mathbf{u}}(\omega) = \mathbf{u}(\omega) e^{-j\phi(\omega)}$ so that the desired component $d(\omega) e^{-j\phi(\omega)}$ becomes real and positive. The resulting real-valued

quantities are

$$\mathbf{r}(\omega) = \Re\{\tilde{\mathbf{u}}(\omega)\}, \quad \mathbf{Q}(\omega) \triangleq \Re\left\{\tilde{\mathbf{u}}(\omega)\tilde{\mathbf{u}}^H(\omega)\right\}.$$

Since $\mathbf{b} \in \{\pm 1\}^N \subset \mathbb{R}^N$ is real, only the symmetric real part contributes, and

$$\mathbf{b}^T \mathbf{Q}(\omega) \mathbf{b} = \left| \tilde{\mathbf{u}}^T(\omega) \mathbf{b} \right|^2 \geq 0.$$

Hence, $\mathbf{Q}(\omega)$ is positive semidefinite in the induced real quadratic form used throughout.

Analogous definitions apply to each interferer m , using $\phi_m(\omega) = \arg(d_m(\omega))$. This rotation simplifies subsequent derivations since all cross terms between the direct and reflected signals become real-valued, and the SINR expression can be presented in a purely real form without loss of generality.

To express the received signal in a compact quadratic form, define the following real-valued coefficients for each random realization ω :

$$\begin{aligned} A(\omega) &= |d(\omega)|^2, B(\mathbf{b}, \omega) = 2\rho|d(\omega)|\mathbf{b}^T \mathbf{r}(\omega), C(\mathbf{b}, \omega) \\ &= \rho^2 \mathbf{b}^T \mathbf{Q}(\omega) \mathbf{b}. \end{aligned} \quad (5)$$

Analogous quantities $A_m(\omega)$, $B_m(\mathbf{b}, \omega)$, and $C_m(\mathbf{b}, \omega)$ are defined for each interferer m as follows:

$$\begin{aligned} A_m(\omega) &= |d_m(\omega)|^2, \quad B_m(\mathbf{b}, \omega) = 2\rho|d_m(\omega)|\mathbf{b}^T \mathbf{r}_m(\omega) \\ C_m(\mathbf{b}, \omega) &= \rho^2 \mathbf{b}^T \mathbf{Q}_m(\omega) \mathbf{b}. \end{aligned} \quad (6)$$

The noise terms introduced earlier on the receiver-side provide the random coefficients

$$D_0(\omega) = N_0 \|\mathbf{w}\|_2^2 + \sigma_{\min}^2 L(\omega), \quad D_1(\omega) = \eta L(\omega),$$

where $L(\omega) = \|\mathbf{H}_r^H(\omega) \mathbf{w}\|_2^2$ is the folded gain factor that links the RIS to the combiner.

Combining all components, the instantaneous SINR for a given binary configuration \mathbf{b} and amplification gain g is expressed compactly as

$$S(\mathbf{b}, g; \omega) \triangleq A(\omega) + gB(\mathbf{b}, \omega) + g^2C(\mathbf{b}, \omega), \quad (7)$$

$$I(\mathbf{b}, g; \omega) \triangleq \sum_{m=1}^M P_m \left(A_m(\omega) + gB_m(\mathbf{b}, \omega) + g^2C_m(\mathbf{b}, \omega) \right), \quad (8)$$

$$\text{SINR}(\mathbf{b}, g; \omega) = \frac{P_d S(\mathbf{b}, g; \omega)}{D_0(\omega) + D_1(\omega)g^2 + I(\mathbf{b}, g; \omega)}. \quad (9)$$

Equation (9) follows by expanding the squared magnitudes of the effective channels in (4) to obtain the quadratic forms in (5)–(6), and by using the folded-noise variance expression in (3) (and its i.i.d. specialization). The full algebraic steps are provided in Appendix A.

Substituting the above definitions yields an SINR expression in quadratic form, which explicitly links the binary phase configuration \mathbf{b} and the active gain g to stochastic fading, cochannel interference, and gain-dependent noise. This compact representation serves as the basis for the chance-constrained optimization developed in Sec. III.

The amplification factor g is subject to both circuit stability and regulatory emission limits. From a small-signal perspective, each RIS element behaves as a two-port device; satisfying the Rollett stability conditions ($K_R > 1$, $|\Delta| < 1$) imposes an upper bound on the realizable gain:

$$0 \leq g \leq g_{\text{stab}} \triangleq \mu \text{MAG},$$

where MAG denotes the maximum available gain of the cell, and $\mu \in (0, 1)$ is a chosen safety factor that maintains stability margins under manufacturing or temperature variations. In addition to stability, the effective isotropic radiated power (EIRP) from each RIS cell must satisfy regulatory emission constraints. With equal-gain two-state reflection ($\alpha = \rho g$), the instantaneous reradiated power of element i is $\rho^2 g^2 \Psi_i(\omega)$, where the random incident power in one coherence block is

$$\Psi_i(\omega) = P_d |\mathbf{g}_{t,i}^\top(\omega) \mathbf{f}|^2 + \sum_{m=1}^M P_m |\mathbf{g}_{t,m,i}^\top(\omega) \mathbf{f}_m|^2.$$

Therefore, enforcing the per-cell emission limit P_{cell}^{\max} requires

$$\rho^2 g^2 \Psi_i(\omega) \leq P_{\text{cell}}^{\max}, \quad \forall i, \forall \omega.$$

Because $\Psi_i(\omega)$ is random (through stochastic propagation and interference), the gain constraint on g is imposed using one of the following statistically conservative formulations. Define the worst-cell incident power as

$$\Psi_{\max}(\omega) \triangleq \max_{i=1,\dots,N} \Psi_i(\omega).$$

1) *Sample-wise worst-case (scenario-robust) bound:* Using the same S samples $\{\omega_s\}_{s=1}^S$ as in the SAA, enforce the EIRP constraint for every sampled realization:

$$g_{\text{EIRP,wc}}^{(S)} = \frac{\sqrt{P_{\text{cell}}^{\max}}}{\rho \sqrt{\max_{s=1,\dots,S} \Psi_{\max}(\omega_s)}}. \quad (10)$$

2) *A quantile (chance-constrained) bound:* an outage level $\alpha \in (0, 1)$ is permitted such that $\Pr\{\rho^2 g^2 \Psi_{\max}(\omega) \leq P_{\text{cell}}^{\max}\} \geq 1 - \alpha$. Let $q_{1-\alpha}$ denote the $(1 - \alpha)$ quantile of $\Psi_{\max}(\omega)$; then

$$g_{\text{EIRP,1-\alpha}} = \frac{\sqrt{P_{\text{cell}}^{\max}}}{\rho \sqrt{q_{1-\alpha}}}. \quad (11)$$

3) *Moment-based (Cantelli) bound*: when only the first two moments of $\Psi_{\max}(\omega)$ are known, Cantelli's inequality provides a closed-form, safe bound.

$$g_{\text{EIRP,Cantelli}} = \frac{\sqrt{P_{\text{cell}}^{\max}}}{\rho \sqrt{\mu_{\max} + c_{\alpha} \sigma_{\max}}}, \quad c_{\alpha} = \sqrt{\frac{1-\alpha}{\alpha}}. \quad (12)$$

where μ_{\max} and σ_{\max} are the means and standard deviations of $\Psi_{\max}(\omega)$, respectively.

The admissible gain must satisfy both the small-signal stability requirement and the selected EIRP constraint, leading to the overall range

$$0 \leq g \leq g_{\max} = \min\{g_{\text{stab}}, g_{\text{EIRP}}\}. \quad (13)$$

where g_{EIRP} corresponds to one of the bounds above, chosen according to the desired reliability level.

This system model unifies random satellite geometry, cochannel interference, and hardware-imposed gain limits within a single stochastic framework. In contrast to deterministic or average-link formulations, (9) makes explicit how random fading, gain-dependent RIS amplifier noise, and interference jointly determine the instantaneous SINR over each coherence block, while (13) enforces physically admissible amplification through stability and EIRP constraints. This stochastic representation enables the reliability-aware, chance-constrained optimization developed in Sec. III and provides a physically consistent foundation for the SAA–MISOCP formulation.

Folded RIS–Amplifier Noise (Stochastic).: We now characterize how RIS amplifier noise propagates through the cascaded channel and determines the stochastic coefficients $D_0(\omega)$ and $D_1(\omega)$ in the SINR denominator. This connection is essential because these coefficients encapsulate the total noise power observed at the receiver, thereby determining the achievable reliability for any feasible RIS gain g . By quantifying how spatial correlation and gain-dependent amplification modify the effective noise, this section provides a statistical link between the RIS hardware behaviour and the stochastic optimization model developed earlier.

We model the per-element amplifier noise as a zero-mean proper complex vector $\mathbf{n}_{\text{RA}}(\omega) \in \mathbb{C}^N$ with covariance

$$\mathbb{E}[\mathbf{n}_{\text{RA}}(\omega)] = \mathbf{0}, \quad \mathbb{E}[\mathbf{n}_{\text{RA}}(\omega) \mathbf{n}_{\text{RA}}^H(\omega)] = \Sigma_a(g, \omega) \succeq \mathbf{0}, \quad (14)$$

independent of the transmitted data symbols $\{x, x_m\}$ and the receiver noise \mathbf{n}_r .

Before proceeding, we briefly outline the structure of this subsection to clarify the modeling logic. We first characterize how the internal amplifier noise scales with the RIS gain g , which

forms the basis of the gain-dependent covariance model. Next, we analyze how this noise component is propagated through the RIS–receiver channel and folded at the combiner output, leading to the expressions for the random coefficients $D_0(\omega)$ and $D_1(\omega)$ in the SINR denominator. Finally, we establish analytical bounds and special cases that connect this general stochastic model to the commonly used i.i.d. and diagonal noise assumptions.

Gain dependence.: The internal noise generated by RIS amplifiers increases with operating gain. We model the amplifier-noise covariance as

$$\Sigma_a(g, \omega) = \Sigma_{\min}(\omega) + g^2 \Sigma_{\text{ex}}(\omega), \quad (15)$$

where $\Sigma_{\min}(\omega) \succeq \mathbf{0}$ is the gain-independent baseline covariance and $\Sigma_{\text{ex}}(\omega) \succeq \mathbf{0}$ is the gain-dependent excess covariance. This PSD affine model covers i.i.d., diagonal, and correlated amplifier-noise structures in a unified form.

Unless stated otherwise, simulations and the SAA formulation use the i.i.d. specialization $\Sigma_{\min}(\omega) = \sigma_{\min}^2 \mathbf{I}$ and $\Sigma_{\text{ex}}(\omega) = \eta \mathbf{I}$, so that $\Sigma_a(g, \omega) = (\sigma_{\min}^2 + \eta g^2) \mathbf{I}$. Under this specialization, (19) reduces to the scalar coefficients used in (9) and Table II.

Folded variance at the receiver.: After propagation through the RIS–receiver channel $\mathbf{H}_r(\omega)$ and combining by \mathbf{w} , the amplifier noise folds to the output with variance

$$\text{Var}_\omega(\mathbf{w}^H \mathbf{H}_r(\omega) \mathbf{n}_{\text{RA}}(\omega)) = \mathbf{w}^H \mathbf{H}_r(\omega) \Sigma_a(g, \omega) \mathbf{H}_r^H(\omega) \mathbf{w}. \quad (16)$$

Using (15), this separates into a gain-independent part and a gain-dependent part:

$$D_{0,\text{RA}}(\omega) = \mathbf{w}^H \mathbf{H}_r(\omega) \Sigma_{\min}(\omega) \mathbf{H}_r^H(\omega) \mathbf{w}, \quad (17)$$

$$D_{1,\text{RA}}(\omega) = \mathbf{w}^H \mathbf{H}_r(\omega) \Sigma_{\text{ex}}(\omega) \mathbf{H}_r^H(\omega) \mathbf{w}. \quad (18)$$

Adding the receiver thermal noise yields the random denominator coefficients

$$D_0(\omega) = N_0 \|\mathbf{w}\|_2^2 + D_{0,\text{RA}}(\omega), \quad D_1(\omega) = D_{1,\text{RA}}(\omega), \quad (19)$$

so the total noise term in (9) is $D_0(\omega) + g^2 D_1(\omega)$.

Geometric interpretation (Rayleigh–Ritz bounds).: To gain intuition about how the RIS channel geometry influences the folded amplifier noise, we employ a Rayleigh–Ritz characterization. This approach expresses each quadratic form $\mathbf{w}^H \mathbf{H}_r(\omega) \mathbf{A} \mathbf{H}_r^H(\omega) \mathbf{w}$ in terms of its principal eigenvalues and the effective channel alignment of the receive combiner. Specifically, let

$$L(\omega) \triangleq \|\mathbf{H}_r^H(\omega) \mathbf{w}\|_2^2 = \mathbf{w}^H \mathbf{H}_r(\omega) \mathbf{H}_r^H(\omega) \mathbf{w}$$

represent the squared channel projection between the RIS and the receiver. For any positive semidefinite matrix $\mathbf{A} \succeq \mathbf{0}$, the Rayleigh–Ritz inequality gives

$$\lambda_{\min}(\mathbf{A}) L(\omega) \leq \mathbf{w}^H \mathbf{H}_r(\omega) \mathbf{A} \mathbf{H}_r^H(\omega) \mathbf{w} \leq \lambda_{\max}(\mathbf{A}) L(\omega).$$

Applying this relation to the covariance matrices $\Sigma_{\min}(\omega)$ and $\Sigma_{\text{ex}}(\omega)$ yields the corresponding bounds on the folded noise terms:

$$\begin{aligned} \lambda_{\min}(\Sigma_{\min}(\omega)) L(\omega) &\leq D_{0,\text{RA}}(\omega) \leq \lambda_{\max}(\Sigma_{\min}(\omega)) L(\omega), \\ \lambda_{\min}(\Sigma_{\text{ex}}(\omega)) L(\omega) &\leq D_1(\omega) \leq \lambda_{\max}(\Sigma_{\text{ex}}(\omega)) L(\omega). \end{aligned} \quad (20)$$

These inequalities show that the scalar $L(\omega)$ quantifies the effective alignment between the combiner and the RIS channel, while the eigenvalue spreads of $\Sigma_{\min}(\omega)$ and $\Sigma_{\text{ex}}(\omega)$ determine how hardware noise correlation scales the baseline and gain-dependent components.

Special cases.: The Rayleigh–Ritz relations in (20) provide general bounds that apply to any positive semidefinite covariance matrices $\Sigma_{\min}(\omega)$ and $\Sigma_{\text{ex}}(\omega)$. To interpret these results more concretely and connect the stochastic model to practical RIS implementations, we now examine several representative covariance structures. Each case corresponds to a different level of spatial correlation among RIS amplifiers and illustrates how the folded noise coefficients $D_0(\omega)$ and $D_1(\omega)$ simplify under specific assumptions.

1) i.i.d. equal-variance model: When all RIS amplifiers produce independent and identically distributed noise with equal power, the covariance matrices reduce to $\Sigma_{\min}(\omega) = \sigma_{\min}^2 \mathbf{I}$ and $\Sigma_{\text{ex}}(\omega) = \eta \mathbf{I}$. Substituting these forms into (19) gives

$$D_0(\omega) = N_0 \|\mathbf{w}\|_2^2 + \sigma_{\min}^2 L(\omega), \quad D_1(\omega) = \eta L(\omega),$$

which reproduces the familiar scalar law widely used in deterministic analyses. In this setting, all RIS elements contribute equally to the folded noise.

2) Element-dependent, uncorrelated model: If each RIS element has a distinct amplifier with a different noise variance but remains uncorrelated with the others, the covariance matrices become diagonal:

$$\Sigma_{\min}(\omega) = \text{diag}\{\sigma_{\min,1}^2, \dots, \sigma_{\min,N}^2\}, \quad \Sigma_{\text{ex}}(\omega) = \text{diag}\{\eta_1, \dots, \eta_N\}.$$

In this case,

$$D_{0,\text{RA}}(\omega) = \sum_{i=1}^N \sigma_{\min,i}^2(\omega) |\mathbf{w}^H \mathbf{h}_{r,i}(\omega)|^2,$$

$$D_1(\omega) = \sum_{i=1}^N \eta_i(\omega) |\mathbf{w}^H \mathbf{h}_{r,i}(\omega)|^2,$$

where $\mathbf{h}_{r,i}(\omega)$ denotes the i -th column of $\mathbf{H}_r(\omega)$. This configuration reveals how spatially varying amplifier quality weights each RIS path according to its coupling with the receiver.

3) Correlated amplifier noise: In practical RIS hardware, mutual coupling and shared bias networks often induce correlations among the amplifiers. The general formulation (16)–(20) then applies with arbitrary positive-semidefinite $\Sigma_{\min}(\omega)$ and $\Sigma_{\text{ex}}(\omega)$. This case captures spatially structured noise fields and allows for the analysis of how correlation among RIS elements modifies the effective noise floor, potentially tightening or relaxing the SINR constraints depending on the dominant eigenmodes of the covariance matrices.

Sample use in SAA.: The quantities $D_0(\omega)$ and $D_1(\omega)$ derived above enter directly into the chance-constrained formulation of the optimization problem (Sec. III). For each sampled realization ω_s of the random environment, these quantities are evaluated as follows:

$$D_{0,s} = D_0(\omega_s), \quad D_{1,s} = D_1(\omega_s),$$

using the definitions in (19). In this way, every scenario in the sample-average approximation (SAA) inherits a distinct noise realization that reflects the specific RIS geometry, receiver combiner, and amplifier correlation structure of that sample.

Under standard scenario-sampling assumptions—i.i.d. samples $\{\omega_s\}_{s=1}^S$, finite moments of the random coefficients (e.g., $\mathbb{E}\|\mathbf{H}_r(\omega)\|_F^2 < \infty$), and uniformly bounded eigenvalues of $\Sigma_{\min}(\omega)$ and $\Sigma_{\text{ex}}(\omega)$ —the sample averages converge to their population values as $S \rightarrow \infty$. Therefore, the SAA constraints become an increasingly accurate *empirical* approximation of the original chance-constrained problem.

Because the resulting program is mixed-integer and relies on Big- M activation, McCormick envelopes, and SOC reformulations, feasibility at finite S should be interpreted as an empirical guarantee on the training scenarios, not as an exact probabilistic certificate. To evaluate reliability, we test the returned design on an independent out-of-sample Monte Carlo set $\{\tilde{\omega}_r\}_{r=1}^{S_{\text{test}}}$ and report

$$\hat{p}_{\text{succ}} = \frac{1}{S_{\text{test}}} \sum_{r=1}^{S_{\text{test}}} \mathbf{1}\{\text{SINR}(\mathbf{b}^{\star}, g^{\star}; \tilde{\omega}_r) \geq \tau^{\star}\},$$

optionally with a binomial confidence interval.

These properties confirm that the stochastic formulation of $D_0(\omega)$ and $D_1(\omega)$ provides a physically consistent basis for the chance-constrained design developed in Sec. III.

Overall, the resulting SAA–MISOCP solution $(\mathbf{b}^*, g^*, \tau^*)$ bridges physical randomness (fading, interference, and folded amplifier noise) and reliability-driven system design by targeting the requirement $\Pr\{\text{SINR}(\mathbf{b}^*, g^*; \omega) \geq \tau^*\} \geq 1 - \varepsilon$ (up to the sampling accuracy of the SAA), while respecting the admissible gain interval $0 \leq g \leq g_{\max}$ imposed by stability and EIRP limits in (13). From an engineering viewpoint, this yields a quantifiable reliability–gain trade-off: increasing g can strengthen the RIS-assisted component and improve coverage, but it also increases the gain-dependent folded-noise contribution through $D_1(\omega)$ and reduces feasibility margins under interference and emission constraints; conversely, smaller gains mitigate self-induced noise amplification and typically improve robustness across stochastic realizations. This interpretation motivates the ceiling analysis and envelope bounds in Sec. IV, which clarify when active amplification is beneficial and when noise- and interference-limited saturation dominates.

III. STOCHASTIC PROBLEM FORMULATION AND SAA–MISOCP

In realistic satellite downlinks, fading and cochannel interference vary randomly across coherence blocks, so deterministic optimization cannot guarantee consistent link quality. To enforce reliability, we require the instantaneous SINR to exceed a target threshold τ with high probability $1 - \varepsilon$, where $\varepsilon \in (0, 1)$ denotes the allowable outage level (e.g., $\varepsilon = 0.1$ corresponds to 90% reliability). The design objective is therefore to determine the binary RIS configuration \mathbf{b} and the amplifier gain g that maximize this guaranteed SINR level.

With all channels being random, the coefficients $A, B, C, A_m, B_m, C_m, D_0, D_1$ in (9) become random functions of ω . For any fixed (\mathbf{b}, g) , $\text{SINR}(\mathbf{b}, g; \omega)$ is a random variable.

To ensure reliability under random channel variations, the design aims to maximize the guaranteed SINR threshold τ subject to an allowable outage probability $\varepsilon \in (0, 1)$. Specifically, the objective is to find the binary RIS configuration \mathbf{b} and the gain g that achieve

$$\begin{aligned} & \max_{\mathbf{b} \in \{\pm 1\}^N, 0 \leq g \leq g_{\max}} \tau \\ \text{s.t. } & \Pr\{\text{SINR}(\mathbf{b}, g; \omega) \geq \tau\} \geq 1 - \varepsilon. \end{aligned} \tag{21}$$

This optimization ensures that, with probability at least $1 - \varepsilon$, the instantaneous SINR exceeds the target τ over the random channel realizations. Although problem (21) is generally non-

Table II
PER-SAMPLE STOCHASTIC COEFFICIENTS FOR SAA (SCENARIO ω_s).

Coefficient	Definition at $\omega = \omega_s$
A_s	$ d(\omega_s) ^2$
$B_s(\mathbf{b})$	$2\rho d(\omega_s) \mathbf{b}^\top \mathbf{r}(\omega_s)$
$C_s(\mathbf{b})$	$\rho^2 \mathbf{b}^\top \mathbf{Q}(\omega_s) \mathbf{b}$
$A_{m,s}$	$ d_m(\omega_s) ^2$
$B_{m,s}(\mathbf{b})$	$2\rho d_m(\omega_s) \mathbf{b}^\top \mathbf{r}_m(\omega_s)$
$C_{m,s}(\mathbf{b})$	$\rho^2 \mathbf{b}^\top \mathbf{Q}_m(\omega_s) \mathbf{b}$
$L(\omega_s)$	$\ \mathbf{H}_r^H(\omega_s) \mathbf{w}\ _2^2$
$D_{0,s}$	$N_0 \ \mathbf{w}\ _2^2 + \sigma_{\min}^2 L(\omega_s)$
$D_{1,s}$	$\eta L(\omega_s)$

convex and analytically intractable, it can be effectively approximated using the sample-average approximation (SAA) framework, which provides empirical probabilistic guarantees when the number of samples is sufficiently large.

To construct the SAA, we first generate S independent and identically distributed (i.i.d.) channel realizations $\{\omega_s\}_{s=1}^S$ that represent possible random environments, including fading, elevation angles, and noise realizations. For each scenario s , the stochastic coefficients $\{A_s, B_s(\mathbf{b}), C_s(\mathbf{b}), A_{m,s}, B_{m,s}(\mathbf{b}), C_{m,s}(\mathbf{b})\}$ are obtained by evaluating the definitions in Sec. II at the sampled realization $\omega = \omega_s$. For convenience, Table II summarizes the per-sample coefficients used in the SAA constraints.

The folding factor $L(\omega_s)$ quantifies how the RIS–receiver channel and the combiner project the spatial amplifier-noise field into the receiver output. For each sample, these coefficients fully determine the instantaneous SINR under (9) and serve as deterministic inputs to the SAA optimization.

At a given SINR threshold τ , the per-sample feasibility condition becomes

$$P_d(A_s + g B_s(\mathbf{b}) + g^2 C_s(\mathbf{b})) \geq \tau$$

$$\left(D_{0,s} + D_{1,s} g^2 + \sum_{m=1}^M P_m (A_{m,s} + g B_{m,s}(\mathbf{b}) + g^2 C_{m,s}(\mathbf{b})) \right). \quad (22)$$

This inequality ensures that the instantaneous SINR requirement is met for the s -th scenario. To impose the overall chance constraint $\Pr\{\cdot\} \geq 1 - \varepsilon$, no more than $\kappa = \lfloor \varepsilon S \rfloor$ samples are

permitted to violate it. Binary indicator variables $v_s \in \{0, 1\}$ mark these potential violations, leading to the joint conditions

$$\underbrace{\sum_{s=1}^S v_s \leq \kappa}_{\text{violation budget}}, \underbrace{\mathcal{E}_s(\mathbf{y}, \mathbf{s}, \mathbf{u}, g, t, \mathbf{z}, \mathbf{Z}; \tau) \geq -M_{\text{big}} v_s}_{\text{Big-}M \text{ activation}}, \quad (23)$$

where $\mathcal{E}_s(\cdot; \tau)$ denotes the linearized form of (22). In the bisection oracle, M_{big} is evaluated (or safely upper-bounded) for each queried value of τ .

The Big-M constant is chosen as a conservative upper bound on the worst-case violation of \mathcal{E}_s over the lifted feasible set (equivalently, over $t \in [0, g_{\max}^2]$):

$$M_{\text{big}} = (1 + \eta_M) \max_{s=1, \dots, S} \{ \tau \bar{R}_s - \underline{L}_s \}, \quad \eta_M \in [0.01, 0.05], \quad (24)$$

where \underline{L}_s and \bar{R}_s are valid bounds satisfying

$$\underline{L}_s \leq \inf_{\mathbf{x} \in \mathcal{X}_{\text{lift}}} P_d \mathcal{T}_s(\mathbf{x}; \omega_s), \quad (25)$$

$$\bar{R}_s \geq \sup_{\mathbf{x} \in \mathcal{X}_{\text{lift}}} \left[D_{0,s} + D_{1,s} t + \sum_{m=1}^M P_m \mathcal{T}_{m,s}(\mathbf{x}; \omega_s) \right], \quad (26)$$

with

$$\mathbf{x} \triangleq (\mathbf{y}, \mathbf{s}, \mathbf{u}, g, t, \mathbf{z}, \mathbf{Z}),$$

and $\mathcal{X}_{\text{lift}}$ denoting the lifted feasible set defined by variable bounds, binary restrictions, McCormick envelopes, and SOC/linking constraints. Accordingly, $v_s = 0$ enforces $\mathcal{E}_s \geq 0$, while $v_s = 1$ allows relaxation via $-M_{\text{big}} v_s$, subject to $\sum_{s=1}^S v_s \leq \kappa$.

Let $\mathbf{1} \in \mathbb{R}^N$ denote the length- N all-ones vector. For each sample s , define the auxiliary terms

$$\mathbf{q}_s = \mathbf{Q}(\omega_s) \mathbf{1}, \quad q_{0,s} = \mathbf{1}^\top \mathbf{Q}(\omega_s) \mathbf{1},$$

and, analogously, $\mathbf{q}_{m,s}$ and $q_{0,m,s}$ for each interferer m . Using the binary mapping $b_i = 2y_i - 1$ and introducing the shared auxiliary variables $(\mathbf{s}, \mathbf{u}, g, t, \mathbf{z}, \mathbf{Z})$, the nonlinear feasibility condition (22) becomes *linear* in all decision variables with sample-dependent coefficients:

$$\mathcal{E}_s(\cdot; \tau) \triangleq P_d \mathcal{T}_s(\omega_s) - \tau \left(D_{0,s} + D_{1,s} t + \sum_{m=1}^M P_m \mathcal{T}_{m,s}(\omega_s) \right). \quad (27)$$

where

$$\begin{aligned}\mathcal{T}_s(\omega_s) &\triangleq A_s - 2\rho|d(\omega_s)|g\mathbf{1}^\top\mathbf{r}(\omega_s) + 4\rho|d(\omega_s)|\mathbf{r}^\top(\omega_s)\mathbf{u} \\ &\quad + \rho^2 q_{0,s} t - 4\rho^2 \mathbf{q}_s^\top \mathbf{z} + 4\rho^2 \sum_{i,j} Q_{s,ij} Z_{ij}, \\ \mathcal{T}_{m,s}(\omega_s) &\triangleq A_{m,s} - 2\rho|d_m(\omega_s)|g\mathbf{1}^\top\mathbf{r}_m(\omega_s) + 4\rho|d_m(\omega_s)|\mathbf{r}_m^\top(\omega_s)\mathbf{u} \\ &\quad + \rho^2 q_{0,m,s} t - 4\rho^2 \mathbf{q}_{m,s}^\top \mathbf{z} + 4\rho^2 \sum_{i,j} Q_{m,s,ij} Z_{ij}.\end{aligned}$$

After expressing each stochastic feasibility condition in the linear form (27), the next objective is to assemble all these sample-wise constraints into a single, tractable optimization program. Because the decision variables include both binary reflection coefficients and continuous amplifier parameters, a mixed-integer convex formulation is required to capture their coupling.

A. Mixed-Integer Conic Feasibility (at fixed τ)

To achieve this integration, we introduce the substitutions $t = g^2$, $b_i = 2y_i - 1$, and $y_i \in \{0, 1\}$. These mappings linearize the quadratic dependence on g and represent the binary reflection states in a continuous form. To handle the remaining bilinear products, auxiliary variables are defined as $s_{ij} = y_i y_j$, $u_i = g y_i$, $z_i = t y_i$, and $Z_{ij} = t s_{ij}$. Under these definitions, each $\mathcal{E}_s(\cdot; \tau)$ in (23)–(27) becomes *affine* in the extended variable set $(\mathbf{y}, \mathbf{s}, \mathbf{u}, g, t, \mathbf{z}, \mathbf{Z})$. This reformulation converts the stochastic nonlinear problem into a form suitable for modern conic optimization solvers.

At this stage, the stochastic feasibility constraints have been fully linearized and expressed in affine form. To render the design computationally tractable, we now proceed through three structured steps. First, we apply convex relaxations to the bilinear terms and enforce the quadratic relations through conic constraints. Next, we assemble all scenario-wise inequalities into a unified sample-average (SAA) feasible set that can be queried by a solver. Finally, we describe the bisection-based MISOCP oracle that searches for the maximum achievable SINR threshold satisfying the prescribed reliability level.

Convex envelopes (McCormick) and SOC link.: Once the bilinear terms are made explicit, convex envelopes are applied to bound them tightly within known variable ranges. The McCormick envelopes for s_{ij} , u_i , z_i , and Z_{ij} remain valid because these variables are sample-

independent and satisfy the uniform bounds $y_i \in [0, 1]$, $g \in [0, g_{\max}]$, and $t \in [0, g_{\max}^2]$. The quadratic relation $t = g^2$ is handled via a rotated SOC relaxation,

$$\|(2g, t - 1)\|_2 \leq t + 1, \quad 0 \leq g \leq g_{\max}, \quad 0 \leq t \leq g_{\max}^2, \quad (28)$$

which guarantee $t \geq g^2$ while preserving convexity and numerical stability. Accordingly, the resulting MISOCP solves a convexified outer approximation of the original bilinear model; the final (\mathbf{b}, g) must be verified through out-of-sample Monte Carlo testing and can be tightened by re-solving with t fixed to g^2 .

SAA chance-feasible set.: With all convex relaxations in place, the entire stochastic design can be written as a single feasibility set that collects all scenario-wise constraints, binary indicators, and convex-linking constraints. For a fixed SINR target τ , define

$$\mathbf{x} \triangleq (\mathbf{y}, g, t, \mathbf{s}, \mathbf{u}, \mathbf{z}, \mathbf{Z}, \mathbf{v}).$$

$$C_S(\tau) \triangleq \left\{ \mathbf{x} \left| \begin{array}{l} \mathcal{E}_s(\mathbf{x}; \tau) \geq -M_{\text{big}} v_s, \quad s = 1, \dots, S, \\ \sum_{s=1}^S v_s \leq \kappa, \\ \text{all McCormick envelope constraints hold,} \\ \text{the rotated-SOC linking constraint holds,} \\ \mathbf{y} \in \{0, 1\}^N, \quad \mathbf{v} \in \{0, 1\}^S \end{array} \right. \right\}. \quad (29)$$

The rotated-SOC linking constraint is given in (28).

Bisection on τ and MISOCP oracle.: Because the feasibility of $C_S(\tau)$ is monotonic in τ (i.e., if $C_S(\tau)$ is feasible, then $C_S(\tau')$ is feasible for any $\tau' \leq \tau$), the largest reliability-guaranteed threshold can be obtained efficiently via scalar bisection. Algorithm 1 summarizes this procedure: at each iteration, we set τ to the midpoint of $[\tau_L, \tau_U]$ and solve the SAA–MISOCP feasibility problem over $C_S(\tau)$. Each feasibility check enforces the sample-wise SINR constraints for all but at most $\kappa = \lfloor \varepsilon S \rfloor$ scenarios, thereby implementing the outage budget of the original chance constraint. If the problem is feasible, τ_L is increased, and the incumbent solution (\mathbf{y}, g) is stored; otherwise, τ_U is decreased. In practice, warm-starting τ_U using a passive (e.g., $g = 0$) or heuristic RIS configuration substantially accelerates convergence and reduces solver runtime.

This procedure returns the largest τ that is feasible for the SAA-based MISOCP approximation at the prescribed violation budget κ . The obtained design is then certified through an out-of-sample Monte Carlo evaluation.

Algorithm 1: SAA-based Reliability Max–SINR via Bisection and MISOCP Feasibility Oracle

Input: Samples $\{\omega_s\}_{s=1}^S$; outage level ε with $\kappa = \lfloor \varepsilon S \rfloor$; gain cap g_{\max} from (13); bisection tolerance ε_τ ; warm-start upper bound $\tau_U^{(0)}$ (e.g., passive/heuristic).

Output: τ^* , \mathbf{b}^* , g^*

Initialize $\tau_L \leftarrow 0$, $\tau_U \leftarrow \tau_U^{(0)}$

Initialize $(\mathbf{y}^{\text{best}}, g^{\text{best}}) \leftarrow (\mathbf{0}, 0)$

while $\tau_U - \tau_L > \varepsilon_\tau$ **do**

$\tau \leftarrow (\tau_L + \tau_U)/2$

// MISOCP feasibility check (oracle): find variables in $C_S(\tau)$

Solve the feasibility problem: find $(\mathbf{y}, g, t, \mathbf{s}, \mathbf{u}, \mathbf{z}, \mathbf{Z}, \mathbf{v}) \in C_S(\tau)$

if feasible **then**

$\tau_L \leftarrow \tau$

Store $(\mathbf{y}^{\text{best}}, g^{\text{best}}) \leftarrow (\mathbf{y}, g)$

else

$\tau_U \leftarrow \tau$

$\tau^* \leftarrow \tau_L$

$\mathbf{b}^* \leftarrow 2\mathbf{y}^{\text{best}} - \mathbf{1}$

$g^* \leftarrow g^{\text{best}}$

// Optional: refine g for fixed \mathbf{b}^* by 1-D search on $[0, g_{\max}]$.

Remarks.: In practice, a conservative yet safe value of M_{big} can be obtained by bounding both sides of (22) at g_{\max} using the eigenvalue limits of $\mathbf{Q}(\omega_s)$ and the norms of $\mathbf{r}(\omega_s)$, which balances numerical robustness and relaxation tightness; overly large M_{big} values can weaken the MILP/MISOCP relaxation and harm solver scalability. If computational complexity becomes critical, the binary indicators in the chance constraint may be replaced by a convex Conditional Value-at-Risk (CVaR) surrogate, which avoids integer variables at the cost of a softer probabilistic guarantee. Finally, McCormick products (s_{ij}, Z_{ij}) need only to be instantiated for indices where $Q_{ij} \neq 0$ occurs in any scenario, significantly reducing the solver's dimensionality.

Complexity considerations.: Relative to the deterministic oracle, the SAA-based MISOCP introduces S additional affine constraints of the form (27) (one per scenario) and S binary indicator variables $\{v_s\}_{s=1}^S$, together with the violation-budget constraint $\sum_{s=1}^S v_s \leq \kappa$ where $\kappa = \lfloor \varepsilon S \rfloor$. The McCormick envelopes and the rotated SOC link (28) are sample-independent and are therefore shared across all scenarios. Consequently, the scenario layer scales linearly with S , whereas the McCormick linearization scales on the order of N^2 due to the pairwise products required by $\mathbf{b}^T \mathbf{Q}(\omega_s) \mathbf{b}$ (and similarly for the interferers). In practice, warm-starting τ

from a passive RIS design (e.g., $g = 0$) or from an alternating-optimization baseline significantly accelerates convergence and yields stable runtimes across Monte-Carlo realizations.

Example instance size.: For the largest setting used in Sec. V (i.e., $N = 128$, $S = 200$, and $\varepsilon = 0.1$, hence $\kappa = 20$), each SAA–MISOCP feasibility instance contains $N + S = 328$ binary variables (the RIS states $\mathbf{y} \in \{0, 1\}^N$ and the scenario indicators $\mathbf{v} \in \{0, 1\}^S$). Assuming a dense $\mathbf{Q}(\omega_s)$ so that all bilinear terms are instantiated, the reformulation introduces approximately $2N^2 + 2N + 2 = 33,026$ continuous variables (including $\mathbf{s}, \mathbf{Z}, \mathbf{u}, \mathbf{z}, g, t$) and about $8N^2 + 8N + S + 1 = 132,297$ linear constraints, plus one rotated second-order cone enforcing $t \geq g^2$ and simple bound constraints. If the symmetry/sparsity of $\mathbf{Q}(\omega_s)$ is exploited (e.g., keeping only the upper triangle and omitting zero entries), the $O(N^2)$ counts reduce proportionally. Finally, the overall runtime is proportional to the number of bisection iterations, which is $I_\tau \approx \lceil \log_2((\tau_U - \tau_L)/\varepsilon_\tau) \rceil$ feasibility solves.

IV. PERFORMANCE BOUNDS AND INTERFERENCE-AWARE ANALYSIS

This section derives *realization-wise* deterministic envelopes that bound the instantaneous $\text{SINR}(\mathbf{b}, g)$ for all channel realizations and establishes an interference-aware high-gain SINR ceiling. These closed-form limits translate the stochastic model of Sec. II into interpretable constraints, revealing how the active gain g , the RIS size N , and the cochannel-interference structure fundamentally cap the achievable SINR.

Building on these bounds, we characterize the achievable performance limits and robustness of the proposed system under stochastic channels and gain-dependent amplifier noise. All large- and small-scale propagation effects, including $\mathbf{H}_r(\omega)$ and $\Sigma_a(g, \omega)$, are modeled as random variables.

The instantaneous SINR for any binary RIS reflection pattern \mathbf{b} and amplifier gain $g \in [0, g_{\max}]$ is given in (9). This ratio captures the combined contributions of direct, reflected, and interfering paths, along with the stochastic effects of receiver and amplifier noise.

To obtain tractable performance limits, the coupling coefficients are bounded using norm and eigenvalue inequalities:

$$\begin{aligned} |B(\mathbf{b}, \omega)| &\leq 2\rho|d(\omega)|\|\mathbf{r}(\omega)\|_1, \\ \rho^2\lambda_{\min}(\mathbf{Q}(\omega))N &\leq C(\mathbf{b}, \omega) \leq \rho^2\lambda_{\max}(\mathbf{Q}(\omega))N. \end{aligned} \quad (30)$$

Analogously, for each interferer m ,

$$\begin{aligned} |B_m(\mathbf{b}, \omega)| &\leq 2\rho|d_m(\omega)| \|\mathbf{r}_m(\omega)\|_1, \\ \rho^2 \lambda_{\min}(\mathbf{Q}_m(\omega)) N &\leq C_m(\mathbf{b}, \omega) \leq \rho^2 \lambda_{\max}(\mathbf{Q}_m(\omega)) N. \end{aligned} \quad (31)$$

For compactness, define

$$\begin{aligned} \bar{B}(\omega) &\triangleq 2\rho|d(\omega)| \|\mathbf{r}(\omega)\|_1, \\ \underline{C}(\omega) &\triangleq \rho^2 N \lambda_{\min}(\mathbf{Q}(\omega)), \quad \bar{C}(\omega) \triangleq \rho^2 N \lambda_{\max}(\mathbf{Q}(\omega)), \\ \bar{B}_m(\omega) &\triangleq 2\rho|d_m(\omega)| \|\mathbf{r}_m(\omega)\|_1, \\ \underline{C}_m(\omega) &\triangleq \rho^2 N \lambda_{\min}(\mathbf{Q}_m(\omega)), \quad \bar{C}_m(\omega) \triangleq \rho^2 N \lambda_{\max}(\mathbf{Q}_m(\omega)). \end{aligned} \quad (32)$$

and

$$\begin{aligned} \underline{N}(g, \omega) &\triangleq A(\omega) - g \bar{B}(\omega) + g^2 \underline{C}(\omega), \\ \bar{N}(g, \omega) &\triangleq A(\omega) + g \bar{B}(\omega) + g^2 \bar{C}(\omega), \end{aligned} \quad (33)$$

$$\begin{aligned} \underline{D}(g, \omega) &\triangleq D_0(\omega) + g^2 D_1(\omega) \\ &\quad + \sum_{m=1}^M P_m \left(A_m(\omega) - g \bar{B}_m(\omega) + g^2 \underline{C}_m(\omega) \right), \\ \bar{D}(g, \omega) &\triangleq D_0(\omega) + g^2 D_1(\omega) \\ &\quad + \sum_{m=1}^M P_m \left(A_m(\omega) + g \bar{B}_m(\omega) + g^2 \bar{C}_m(\omega) \right). \end{aligned} \quad (34)$$

Substituting these bounds into (9) yields deterministic realization-wise envelopes:

$$\underline{\text{SINR}}(g; \omega) = \frac{P_d \underline{N}(g, \omega)}{\bar{D}(g, \omega)}, \quad (35)$$

$$\overline{\text{SINR}}(g; \omega) = \frac{P_d \bar{N}(g, \omega)}{\bar{D}(g, \omega)}. \quad (36)$$

Hence, over the admissible gain interval where the lower-envelope denominator is positive,

$$\underline{\text{SINR}}(g; \omega) \leq \text{SINR}(\mathbf{b}, g; \omega) \leq \overline{\text{SINR}}(g; \omega), \quad \forall \mathbf{b} \in \{\pm 1\}^N.$$

This condition is naturally satisfied in physically meaningful operating points because thermal noise contributes a strictly positive term in $D_0(\omega)$. A full derivation is provided in Appendix B.

When g is small, numerical stability can be improved by applying a triangle-inequality bound:

$$(\sqrt{A} - \sqrt{C_{\max}} g)_+^2 \leq A + gB + g^2C \leq (\sqrt{A} + \sqrt{C_{\max}} g)^2,$$

where $C_{\max} = \rho^2 N \lambda_{\max}(\mathbf{Q})$, with analogous expressions for interferers.

High-gain SINR ceiling (interference-aware saturation). A key implication of the gain-dependent folded-noise model is that *increasing g cannot improve SINR beyond a finite limit*. Specifically, as g grows, the quadratic reflection energies $g^2C(\mathbf{b}, \omega)$ and $\{g^2C_m(\mathbf{b}, \omega)\}$ dominate the numerator and the reflected-interference terms, while the folded amplifier-noise contribution $g^2D_1(\omega)$ simultaneously dominates the denominator. Dividing the SINR expression by g^2 therefore yields the realization-wise ceiling

$$\begin{aligned} \lim_{g \rightarrow \infty} \text{SINR}(\mathbf{b}, g; \omega) &= \frac{P_d C(\mathbf{b}, \omega)}{D_1(\omega) + \sum_m P_m C_m(\mathbf{b}, \omega)} \\ &\leq \frac{P_d \rho^2 \lambda_{\max}(\mathbf{Q}(\omega)) N}{D_1(\omega) + \sum_m P_m \rho^2 \lambda_{\min}(\mathbf{Q}_m(\omega)) N}. \end{aligned} \quad (37)$$

Notably, the direct-path and cross terms $A(\omega)$ and $B(\mathbf{b}, \omega)$ vanish in this limit; thus, the high-gain behavior is governed solely by $\{C, C_m\}$ and $D_1(\omega)$.

Active amplification is therefore beneficial compared with passive reflection whenever the asymptotic ceiling in (37) exceeds the passive SINR

$$\frac{P_d A(\omega)}{D_0(\omega) + \sum_{m=1}^M P_m A_m(\omega)}.$$

A sufficient condition for this improvement is

$$\frac{P_d \rho^2 \lambda_{\max}(\mathbf{Q}(\omega)) N}{D_1(\omega) + \sum_{m=1}^M P_m \rho^2 \lambda_{\min}(\mathbf{Q}_m(\omega)) N} > \frac{P_d A(\omega)}{D_0(\omega) + \sum_{m=1}^M P_m A_m(\omega)}. \quad (38)$$

Averaging or percentile evaluation of this inequality across channel realizations provides design guidelines for the expected performance benefits or outages that result from the operation of the active RIS.

The pathwise envelopes (35)–(36) and the high-gain ceiling (37) describe how the instantaneous SINR varies across random realizations of the RIS channel and amplifier noise. However, these scenario-specific results do not, by themselves, guarantee a prescribed level of reliability when the environment fluctuates. To translate these findings into a robust and certifiable design framework, the analysis proceeds in three stages: (i) we formulate a reliability-aware optimization that enforces the SINR constraint with a specified probability; (ii) we extract interpretable scaling laws that reveal how physical parameters govern stochastic performance; and (iii) we outline verification metrics to certify and interpret the obtained design.

(i) *Chance-Constrained Design (Recap)*: The complete reliability-aware optimization framework is presented in Sec. III. There, we maximize the guaranteed SINR threshold τ under the chance constraint

$$\Pr\{\text{SINR}(\mathbf{b}, g; \omega) \geq \tau\} \geq 1 - \varepsilon,$$

with $\mathbf{b} \in \{\pm 1\}^N$ and $0 \leq g \leq g_{\max}$. The probabilistic constraint is approximated by SAA using S scenarios and violation budget $\kappa = \lfloor \varepsilon S \rfloor$, and solved via bisection with an MISOCP feasibility oracle (Algorithm 1). Accordingly, this section does not repeat those derivations; instead, it uses the resulting solution $(\mathbf{b}^*, g^*, \tau^*)$ to interpret the envelope bounds in (35)–(36) and the high-gain ceiling in (37).

(ii) *Interpretable Scaling Laws (Stochastic Regime)*: Before moving to numerical validation, it is useful to extract analytical trends from the stochastic envelopes. Equations (35)–(36) and (37) reveal how system parameters influence reliable SINR.

- **RIS size (N)**: Desired and interfering reflections scale respectively with $\rho^2 N \lambda_{\max}(\mathbf{Q})$ and $\rho^2 N \lambda_{\min}(\mathbf{Q}_m)$. Increasing N widens the SINR range but can magnify interference if eigenstructures align.
- **Eigenstructure**: Strong alignment of the desired LoS component (large $\lambda_{\max}(\mathbf{Q})$) and weak alignment of interferers (small $\lambda_{\min}(\mathbf{Q}_m)$) elevate the SINR ceiling and enhance robustness.
- **Gain-dependent noise**: The excess-noise coefficient $D_1(\omega)$ limits the SINR ceiling at large g . Strong folding gain $L(\omega)$ or correlated amplifier noise (large eigenvalues of $\Sigma_{\text{ex}}(\omega)$) reduces the benefit of active gain.
- **Outage sensitivity**: Stricter reliability (smaller ε) shifts the feasible τ toward the lower envelope (35), illustrating the trade-off between guaranteed SINR and allowable risk.

(iii) *Verification and Reporting Metrics*: To assess the robustness and interpretability of the obtained design, Monte–Carlo testing is performed on an independent test set $\{\tilde{\omega}_r\}_{r=1}^{S_{\text{test}}}$ using the optimized parameters $(\mathbf{b}^*, g^*, \tau^*)$. Three complementary diagnostic metrics are employed:

- 1) **Empirical reliability**: The achieved reliability is estimated as

$$\hat{p}_{\text{succ}} = \frac{1}{S_{\text{test}}} \sum_{r=1}^{S_{\text{test}}} \mathbb{1}\{\text{SINR}(\mathbf{b}^*, g^*; \tilde{\omega}_r) \geq \tau^*\}.$$

which approximates the true non-outage probability.

- 2) **SINR statistics**: Report the empirical mean, variance, and $(1-\varepsilon)$ -quantile of $\text{SINR}(\mathbf{b}^*, g^*; \omega_s)$, confirming that τ^* lies near the target quantile boundary.

3) **Ceiling gap:** Evaluate the scenario-wise ceiling (37) to quantify how far the achieved SINR operates below the theoretical high-gain limit.

Together, these diagnostics validate the probabilistic design guarantees and link the stochastic optimization outcomes to the physical RIS–satellite model developed in Sections II–III.

V. NUMERICAL RESULTS AND DISCUSSIONS

This section validates the stochastic framework by confronting its analytical envelopes, gain ceilings, and chance-constrained design with Monte–Carlo evidence generated under the Rician block-fading channel model in (1), the instantaneous SINR model in (9), and the folded-noise law in (19). We first list the parameters used consistently across the figures; then, we build the discussion progressively: we begin with a quantile performance view versus the interference load (validating **C1**), then move to the gain–reliability tradeoff in a per-panel analysis that reveals the ceiling mechanism (validating **C3**), and finally quantify the reliability-guaranteed surface over (N, M) at fixed gains (validating **C2**, **C4**). Throughout, the admissible gain interval strictly respects the stability–EIRP cap (13) instantiated via (10)–(12).

Unless otherwise stated, all simulations follow the stochastic model in Sec. II with Rician block fading (1), folded-noise coefficients (19), and the admissible gain cap g_{\max} from (13). We use $S = 200$ i.i.d. stochastic realizations per configuration and target outage $\varepsilon = 0.1$ (i.e., 90% non-outage), so the SAA violation budget is $\kappa = \lfloor \varepsilon S \rfloor = 20$. Table III lists all default parameters and sweep ranges.

To connect the normalized parameters to a representative satellite link budget, we consider a Ka-band downlink with a carrier frequency $f_c = 20$ GHz and a bandwidth $B = 100$ MHz, as well as a LEO altitude (satellite–ground distance scale) of $h = 400$ km. The receiver thermal-noise power over bandwidth B is $N_{\text{th}} = kTB$, and with a noise figure F (linear, corresponding to NF in dB), the effective noise becomes $N_{\text{eff}} = kTB F$. Throughout the simulations, we normalize the receiver noise variance to $N_0 = 1$; thus, all reported SINR values can be mapped to absolute units by scaling transmit powers by the factor $1/N_{\text{eff}}$ for the chosen (B, NF) . This normalization keeps the stochastic SINR structure (9) unchanged while enabling the physical interpretation of the results.

We begin with Fig. 2, which plots the empirical $(1-\varepsilon)$ –quantile of SINR as a function of the interference load M for several fixed gains g (panels) and RIS sizes N (curves). When $g = 0$, (9) reduces to the passive ratio $\text{SINR} = P_d A / (D_0 + \sum_m P_m A_m)$ with D_0 given by (19), which is

Table III
SIMULATION PARAMETERS USED IN SEC. V (DEFAULTS AND SWEEPS UNLESS STATED).

Symbol	Parameter	Value / Sweep
f_c	Carrier frequency	20 GHz (Ka-band example)
B	System bandwidth	100 MHz
h	LEO altitude / distance scale	400 km
NF	Receiver noise figure	5 dB (used for physical interpretation; simulations use $N_0 = 1$ normalization)
N	RIS elements	{16, 32, 64, 128}
M	Cochannel interferers	{2, 4, 6, 8}
g	Active gain (common)	Panels {0, 0.5, 1, 2}; sweeps [0, g_{\max}]
ρ	Passive retention factor	0.9
P_d	Desired-link power	$P_d = 1$
P_m	Interferer power	$P_m = P_d$
N_0	Receiver noise variance	1 (normalized)
σ_{\min}^2	RIS amplifier baseline noise	0.05
η	Excess-noise coefficient	0.02
K	Rician K -factor	6 (linear)
S	SAA sample size	200
ε	Outage probability	0.10

essentially independent of N ; the only trend is the monotonic degradation with M because the denominator increases additively. This directly reflects the lower/upper envelopes in (35)–(36) specialized to $g = 0$ and thus validates the **C1** claim that the eigenvalue/ ℓ_1 bounds control the entire SINR range path-wise. As soon as $g > 0$, the reflected terms $g B(\mathbf{b}, \omega)$ and $g^2 C(\mathbf{b}, \omega)$ enter the numerator, while $g^2 D_1(\omega)$ appears in the denominator. Because $C(\mathbf{b}, \omega) = \rho^2 \mathbf{b}^\top \mathbf{Q}(\omega) \mathbf{b}$ is confined by $\rho^2 N \lambda_{\min}(\mathbf{Q}) \leq C \leq \rho^2 N \lambda_{\max}(\mathbf{Q})$ from (30), enlarging N reliably shifts the curves upward. Yet, the improvement saturates as g grows because (37) limits the high-gain behavior by the ratio of C -terms to $D_1 + \sum_m P_m C_m$, specifically the flattening observed in the active panels. The figure therefore combines the two pillars of **C1**: (i) path-wise envelopes (35)–(36) tracking the entire gain region, and (ii) the asymptotic ceiling (37) explaining saturation under gain-dependent noise.

The saturation observed at higher gains in Fig. 2 motivates a reliability-centered interpretation,

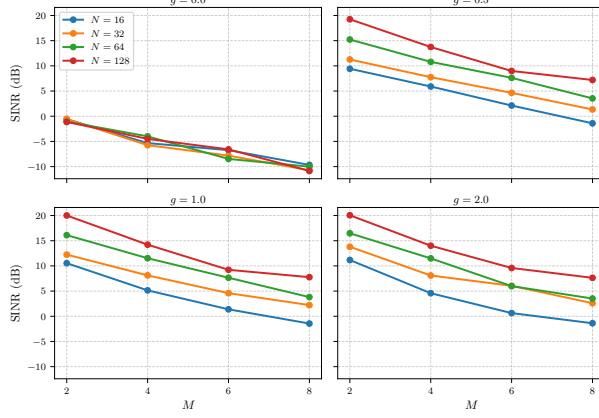


Fig. 2. $(1 - \varepsilon)$ -quantile SINR versus number of interferers M at fixed gains g (panels) and RIS sizes N (curves), computed from (9) under the SAA sampling settings in Table III. The passive baseline ($g = 0$) follows directly from (9), while saturation at larger g is consistent with the high-gain ceiling in (37).

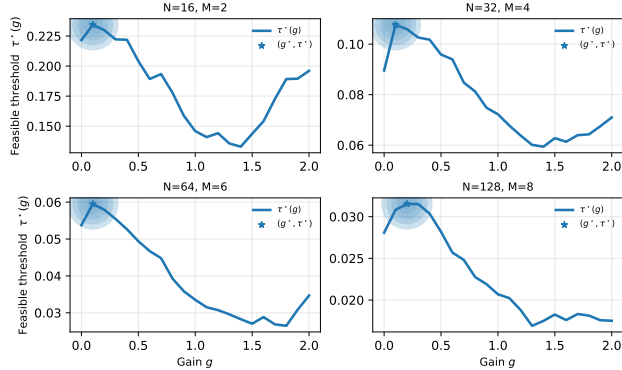


Fig. 3. Reliability-guaranteed SINR threshold $\tau^*(g)$ obtained by the SAA-MISOCP bisection oracle (Algorithm 1) for (21), with sample-wise constraints (22) enforced via (23). The saturation/decline trend at large g is explained by the folded-noise term $g^2 D_1(\omega)$ in (19) and the ceiling behavior in (37).

shown in Fig. 3. For each fixed (N, M) panel and each gain value g , we solve the SAA-MISOCP feasibility problem and report $\tau^*(g)$ as the largest SAA-feasible SINR threshold under the violation budget $\kappa = \lfloor \varepsilon S \rfloor$ in (23). Equivalently, on the SAA training set, at most κ out of S scenarios violate the SINR constraint, so the empirical non-outage level is at least $1 - \kappa/S \approx 1 - \varepsilon$ (up to solver tolerances and the Big- M /McCormick/SOC reformulation). Therefore, at finite S , (21) is targeted empirically rather than certified exactly; the final reliability is validated using independent out-of-sample Monte-Carlo testing.

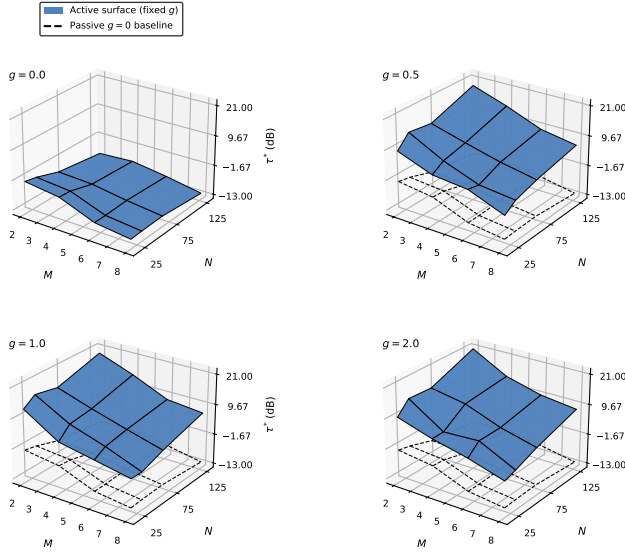


Fig. 4. Reliability-guaranteed SINR surface $\tau^*(N, M; g)$ at fixed gains $g \in \{0, 0.5, 1, 2\}$ obtained for (21) using the SAA-MISOCP model with sample-wise constraints (22) enforced through (23). The scaling with N follows the quadratic-reflection term $C(\mathbf{b}, \omega)$ bounded in (30), while degradation with M follows the additive interference structure in (9).

The trend in $\tau^*(g)$ follows directly from (9). For small g , the numerator is mainly $A(\omega) + gB(\mathbf{b}, \omega)$ while the denominator changes slowly, so choosing \mathbf{b} aligned with $\mathbf{r}(\omega)$ makes $B(\mathbf{b}, \omega)$ positive and yields an initial near-linear increase. As g grows, both desired and interference reflection terms scale as g^2 through $C(\mathbf{b}, \omega)$ and $C_m(\mathbf{b}, \omega)$, and the folded-noise term $g^2 D_1(\omega)$ also increases in the denominator (see (19)). Consequently, $\tau^*(g)$ eventually saturates and may decline, consistent with the ceiling law in (37). Practically, this identifies a useful operating-gain region: beyond it, additional amplification mainly increases internal noise rather than reliable SINR. This behavior supports **C3** and remains consistent with the stochastic-envelope interpretation in **C1**.

Having seen how reliability evolves with g for a given (N, M) , Fig. 4 broadens the view of the entire (N, M) plane at fixed gains. Each surface point is the SAA $(1 - \varepsilon)$ -feasible threshold $\tau^*(N, M; g)$ obtained from (21) using the sample-wise constraints (22) (linearized as (27)) and enforced through (23).

Increasing N lifts the surface due to coherent scaling $C(\mathbf{b}, \omega) \sim \rho^2 N \lambda_{\max}(\mathbf{Q}(\omega))$ in (30), whereas increasing M depresses it through the additive interference term $\sum_{m=1}^M P_m (A_m + gB_m + g^2 C_m)$ in (9). The dashed wireframe at $g = 0$ provides the passive baseline. The clear separation between the active ($g > 0$) and passive ($g = 0$) surfaces visualizes how the proposed stochastic design enables *controlled amplification*: active gain improves the reliability-guaranteed SINR

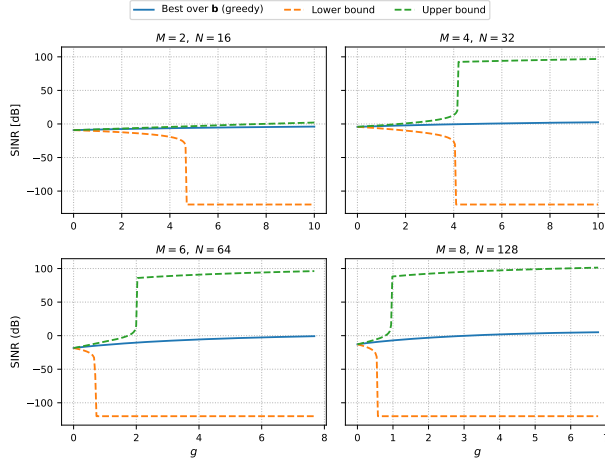


Fig. 5. Envelope consistency across gains: for each realization ω , the path-wise bounds (35)–(36) provably sandwich $\text{SINR}(\mathbf{b}, g; \omega)$ for all \mathbf{b} and $g \in [0, g_{\max}]$. The plotted empirical “best over \mathbf{b} ” curve therefore lies between the two envelopes, validating the bound tightness and the ceiling trend (37).

only within the physically admissible range $0 \leq g \leq g_{\max}$ imposed by stability and EIRP constraints in (13). Regions where the active surfaces lie above the passive wireframe satisfy the sufficient improvement condition (38), confirming that amplification is beneficial precisely when the high-gain ceiling in (37) exceeds the passive ratio $P_d A / D_0$. Since each $(N, M; g)$ point is obtained from the SAA violation budget (with $\kappa = \lfloor \varepsilon S \rfloor$), the figure illustrates the reliability-targeting design and its out-of-sample validation, as well as the **C4** physics–optimization bridge: the SAA constraints (22) are enforced via the Big- M violation-budget formulation (23) with McCormick/SOC convexification, while respecting the gain cap (13).

Finally, Fig. 5 closes the loop by checking that the empirical “best over \mathbf{b} ” curve is indeed sandwiched between the deterministic envelopes predicted by (35)–(36) for all gains in the admissible range $0 \leq g \leq g_{\max}$. At small g , triangle-inequality regularization (as stated after (36)) guarantees nonnegativity and explains the gentle initial slope, while at larger g , all three curves flatten in unison toward the ceiling (37). Because the horizontal axis truncation reflects g_{\max} from (13) (with g_{EIRP} selected via (10), (11), or (12) depending on the reliability posture), the comparison remains physically meaningful and numerically stable. This figure, therefore, provides a direct, per-realization validation of **C1** while reinforcing the ceiling phenomenon of **C3** and the feasibility architecture of **C4**.

Together, Figs. 2–5 validate the model: the SINR envelopes (35)–(36) and ceiling (37) explain the trends over (N, M, g) , while folded noise (19) explains saturation at high g . The reliability

gains predicted by (38) are observed, and the chance-constrained SAA–MISOCP design in (21) (implemented via (22), (27), and (23)) matches Monte-Carlo results across passive/active regimes and low/high interference.

VI. CONCLUSION

This paper proposes a stochastic reliability framework for active RIS–assisted satellite down-links under random fading, cochannel interference, and gain-dependent (folded) amplifier noise. Reliability is enforced through a chance constraint on the instantaneous SINR and is solved via an SAA-based MISOCP feasibility oracle combined with scalar bisection, while explicitly restricting the common gain to the physically admissible interval $0 \leq g \leq g_{\max}$ determined by stability and EIRP limits.

Analytically, we derived realization-wise SINR envelopes and an interference-aware high-gain ceiling that explain the transition from useful amplification to saturation: increasing g strengthens the reflected component only until the quadratic folded-noise term $g^2 D_1(\omega)$ (together with interference-related $g^2 C_m(\mathbf{b}, \omega)$ terms) dominates the denominator. This yields a quantifiable *reliability-gain trade-off* and effectively characterizes the usable gain region for active RIS operation under realistic noise statistics.

Monte-Carlo results corroborated the theory by showing that the envelopes track the simulated SINR behavior across passive and active regimes, capture the observed saturation at higher gains, and reproduce the expected degradation with increasing interference. The resulting reliability-guaranteed surfaces further highlight the separation between passive ($g = 0$) and active ($g > 0$) operation, demonstrating controlled amplification without violating the stability/EIRP-imposed gain cap.

In terms of scalability, each bisection iteration requires one SAA–MISOCP feasibility solve; the scenario layer scales linearly with the sample size S , while the McCormick linearization scales on the order of N^2 due to pairwise bilinear products. Warm-starting from a passive or alternating-optimization baseline reduces iterations and stabilizes runtime across Monte-Carlo realizations. Future work will extend the framework to wideband and multiuser settings, finer phase/gain control, adaptive data-driven operation under time-varying CSI, and experimental validation with hardware prototypes and measured channels.

REFERENCES

- [1] M. Dajer, Z. Ma, L. Piazz, N. Prasad, X.-F. Qi, B. Sheen, J. Yang, and G. Yue, “Reconfigurable intelligent surface: Design the channel – a new opportunity for future wireless networks,” *Digital Communications and Networks*, 2021. [Online]. Available: <https://www.sciencedirect.com/science/article/pii/S2352864821000912>
- [2] Q. Li, M. El-Hajjar, I. Hemadéh, D. Jagyasi, A. Shojaeifard, and L. Hanzo, “Performance analysis of active ris-aided systems in the face of imperfect csi and phase shift noise,” *IEEE Transactions on Vehicular Technology*, vol. 72, no. 6, pp. 8140–8145, 2023.
- [3] E. Basar, M. Di Renzo, J. De Rosny, M. Debbah, M.-S. Alouini, and R. Zhang, “Wireless communications through reconfigurable intelligent surfaces,” *IEEE Access*, vol. 7, pp. 116 753–116 773, 2019.
- [4] Y. Ma, K. Ota, and M. Dong, “Qoe optimization for virtual reality services in multi-ris-assisted terahertz wireless networks,” *IEEE Journal on Selected Areas in Communications*, vol. 42, no. 3, pp. 538–551, 2024.
- [5] I. Yildirim, A. Uyurus, and E. Basar, “Modeling and analysis of reconfigurable intelligent surfaces for indoor and outdoor applications in future wireless networks,” *IEEE Transactions on Communications*, vol. 69, no. 2, pp. 1290–1301, 2021.
- [6] C. Pan, H. Ren, K. Wang, J. F. Kolb, M. Elkashlan, M. Chen, M. Di Renzo, Y. Hao, J. Wang, A. L. Swindlehurst, X. You, and L. Hanzo, “Reconfigurable intelligent surfaces for 6g systems: Principles, applications, and research directions,” *IEEE Communications Magazine*, vol. 59, no. 6, pp. 14–20, 2021.
- [7] M. I. Khalil, J. Lin, and K. Wang, “Improving energy efficiency in satellite-to-ground communications with multiple reflecting intelligent surfaces,” *IEEE Transactions on Green Communications and Networking*, vol. 8, no. 4, pp. 1985–1999, 2024.
- [8] Y. Liu, X. Liu, X. Mu, T. Hou, J. Xu, M. Di Renzo, and N. Al-Dhahir, “Reconfigurable intelligent surfaces: Principles and opportunities,” *IEEE Communications Surveys Tutorials*, vol. 23, no. 3, pp. 1546–1577, 2021.
- [9] Z. Zheng, W. Jing, Z. Lu, X. Wen, Q. Wu, and H. Shao, “Ris-aided hotspot capacity enhancement for multibeam satellite systems,” *IEEE Transactions on Wireless Communications*, vol. 23, no. 4, pp. 3648–3664, 2024.
- [10] M. Toka, B. Lee, J. Seong, A. Kaushik, J. Lee, J. Lee, N. Lee, W. Shin, and H. V. Poor, “Ris-empowered leo satellite networks for 6g: Promising usage scenarios and future directions,” *IEEE Communications Magazine*, vol. 62, no. 11, pp. 128–135, 2024.
- [11] C. Kim, W. Saad, and M. Jung, “Performance analysis of ris-aided multibeam satellite communication systems,” *IEEE Transactions on Aerospace and Electronic Systems*, vol. 60, no. 6, pp. 9383–9393, 2024.
- [12] T. Wang, M.-A. Badiu, G. Chen, and J. P. Coon, “Outage probability analysis of ris-assisted wireless networks with von mises phase errors,” *IEEE Wireless Communications Letters*, vol. 10, no. 12, pp. 2737–2741, 2021.
- [13] G. Zhou, C. Pan, H. Ren, D. Xu, Z. Zhang, J. Wang, and R. Schober, “A framework for transmission design for active ris-aided communication with partial csi,” *IEEE Transactions on Wireless Communications*, vol. 23, no. 1, pp. 305–320, 2024.
- [14] H. Chen, G. Yang, and Y.-C. Liang, “Joint active and passive beamforming for reconfigurable intelligent surface enhanced symbiotic radio system,” *IEEE Wireless Communications Letters*, vol. 10, no. 5, pp. 1056–1060, 2021.
- [15] Z. Zhang, L. Dai, X. Chen, C. Liu, F. Yang, R. Schober, and H. V. Poor, “Active ris vs. passive ris: Which will prevail in 6g?” *IEEE Transactions on Communications*, vol. 71, no. 3, pp. 1707–1725, 2023.
- [16] Z. Zheng, W. Jing, Z. Lu, Q. Wu, H. Zhang, and D. Gesbert, “Cooperative multi-satellite and multi-ris beamforming: Enhancing leo satcom and mitigating leo-geo intersystem interference,” *IEEE Journal on Selected Areas in Communications*, vol. 43, no. 1, pp. 279–296, 2025.

- [17] Q. Wu and R. Zhang, "Intelligent reflecting surface enhanced wireless network via joint active and passive beamforming," *IEEE Transactions on Wireless Communications*, vol. 18, no. 11, pp. 5394–5409, 2019.
- [18] M. I. Khalil, "Enhancing active reconfigurable intelligent surface," *Intelligent and Converged Networks*, vol. 3, no. 4, pp. 351–363, 2022.
- [19] R. Long, Y.-C. Liang, Y. Pei, and E. G. Larsson, "Active reconfigurable intelligent surface-aided wireless communications," *IEEE Transactions on Wireless Communications*, vol. 20, no. 8, pp. 4962–4975, 2021.
- [20] M. H. Khoshafa, T. M. N. Ngatched, M. H. Ahmed, and A. R. Ndjidongue, "Active reconfigurable intelligent surfaces-aided wireless communication system," *IEEE Communications Letters*, vol. 25, no. 11, pp. 3699–3703, 2021.
- [21] H. Chen, N. Li, R. Long, and Y.-C. Liang, "Channel estimation and training design for active ris aided wireless communications," *IEEE Wireless Communications Letters*, vol. 12, no. 11, pp. 1876–1880, 2023.
- [22] C. Obinna Nnamani, C. L. Anioke, S. Al-Rubaye, and A. Tsourdos, "Signal-to-interference-noise-ratio density distribution for uav-carried irs-to-6g ground communication," *IEEE Access*, vol. 13, pp. 49 824–49 835, 2025.
- [23] Z. Yigit and E. Basar, "Hybrid star-ris enabled integrated sensing and communication," *IEEE Transactions on Communications*, vol. 73, no. 9, pp. 8289–8300, 2025.
- [24] W. Khalid, A.-A. A. Boulogerigos, T. Van Chien, J. Lee, H. Lee, and H. Yu, "Optimal operation of active ris-aided wireless powered communications in iot networks," *IEEE Internet of Things Journal*, vol. 12, no. 1, pp. 390–401, 2025.
- [25] L. Dai, B. Wang, M. Wang, X. Yang, J. Tan, S. Bi, S. Xu, F. Yang, Z. Chen, M. D. Renzo, C.-B. Chae, and L. Hanzo, "Reconfigurable intelligent surface-based wireless communications: Antenna design, prototyping, and experimental results," *IEEE Access*, vol. 8, pp. 45 913–45 923, 2020.
- [26] P. Gavriilidis, D. Mishra, B. Smida, E. Basar, C. Yuen, and G. C. Alexandropoulos, "Active reconfigurable intelligent surfaces: Circuit modeling and reflection amplification optimization," *IEEE Open Journal of the Communications Society*, vol. 6, pp. 5693–5711, 2025.
- [27] Q. Zhu, M. Li, R. Liu, Y. Liu, and Q. Liu, "Joint beamforming designs for active reconfigurable intelligent surface: A sub-connected array architecture," *IEEE Transactions on Communications*, vol. 70, no. 11, pp. 7628–7643, 2022.
- [28] G. Zakka El Nashef, F. Torres, S. Mons, T. Reveyrand, T. Monediere, E. Ngoya, and R. Quere, "Em/circuit mixed simulation technique for an active antenna," *IEEE Antennas and Wireless Propagation Letters*, vol. 10, pp. 354–357, 2011.
- [29] L. Wu, Q. Y. Zhou, J. Y. Dai, S. Wang, J. Zhang, Z. J. Qi, H. Yang, R. Jiang, Z. X. Wang, H. Li, Z. Zhang, J. Luo, Q. Cheng, and T. J. Cui, "A wideband amplifying and filtering reconfigurable intelligent surface for wireless relay," *Engineering*, 2025. [Online]. Available: <https://www.sciencedirect.com/science/article/pii/S2095809925003121>
- [30] P. Zeng, D. Qiao, Q. Wu, and Y. Wu, "Throughput maximization for active intelligent reflecting surface-aided wireless powered communications," *IEEE Wireless Communications Letters*, vol. 11, no. 5, pp. 992–996, 2022.
- [31] W. Lv, J. Bai, Q. Yan, and H. M. Wang, "Ris-assisted green secure communications: Active ris or passive ris?" *IEEE Wireless Communications Letters*, vol. 12, no. 2, pp. 237–241, 2023.
- [32] H. Niu, Z. Lin, K. An, X. Liang, Y. Hu, D. Li, and G. Zheng, "Active ris-assisted secure transmission for cognitive satellite terrestrial networks," *IEEE Transactions on Vehicular Technology*, vol. 72, no. 2, pp. 2609–2614, 2023.
- [33] T.-T.-M. Tran, B.-M. Vu, and O.-S. Shin, "Optimization of bandwidth allocation and uav placement in active ris-assisted uav communication networks with wireless backhaul," *Drones*, vol. 9, no. 2, 2025. [Online]. Available: <https://www.mdpi.com/2504-446X/9/2/111>
- [34] C. Pan, G. Zhou, K. Zhi, S. Hong, T. Wu, Y. Pan, H. Ren, M. D. Renzo, A. Lee Swindlehurst, R. Zhang, and A. Y. Zhang, "An overview of signal processing techniques for ris/irs-aided wireless systems," *IEEE Journal of Selected Topics in Signal Processing*, vol. 16, no. 5, pp. 883–917, 2022.

- [35] E. Kim, I. P. Roberts, and J. G. Andrews, “Downlink analysis and evaluation of multi-beam leo satellite communication in shadowed rician channels,” *IEEE Transactions on Vehicular Technology*, vol. 73, no. 2, pp. 2061–2075, 2024.
- [36] G. Zheng, S. Ma, K.-k. Wong, and T.-S. Ng, “Robust beamforming in cognitive radio,” *IEEE Transactions on Wireless Communications*, vol. 9, no. 2, pp. 570–576, 2010.